Article

Deep Flow Variability Offshore South-West Svalbard (Fram Strait)

Manuel Bensi [1,*], **Vedrana Kovačević** [1], **Leonardo Langone** [2], **Stefano Aliani** [2], **Laura Ursella** [1], **Ilona Goszczko** [3], **Thomas Soltwedel** [4], **Ragnheid Skogseth** [5], **Frank Nilsen** [5], **Davide Deponte** [1], **Paolo Mansutti** [1], **Roberto Laterza** [1], **Michele Rebesco** [1], **Leonardo Rui** [1], **Renata Giulia Lucchi** [1], **Anna Wåhlin** [6], **Angelo Viola** [7], **Agnieszka Beszczynska-Möller** [3] and **Angelo Rubino** [8]

[1] OGS—National Institute of Oceanography and Applied Geophysics, 34010 Sgonico, Italy; vkovacevic@inogs.it (V.K.); lursella@inogs.it (L.U.); ddeponte@inogs.it (D.D.); pmansutti@inogs.it (P.M.); rlaterza@inogs.it (R.L.); mrebesco@inogs.it (M.R.); lrui@inogs.it (L.R.); rlucchi@inogs.it (R.G.L.)

[2] CNR–ISMAR—Italian National Research Council, Institute of Marine Sciences, 30122 Venice, Italy; leonardo.langone@bo.ismar.cnr.it (L.L.); stefano.aliani@sp.ismar.cnr.it (S.A.)

[3] IOPAN—Institute of Oceanology Polish Academy of Sciences, 81-712 Sopot, Poland; ilona_g@iopan.gda.pl (I.G.); abesz@iopan.gda.pl (A.B.-M.)

[4] AWI—Alfred Wegener Institute, Helmholtz-Center for Polar and Marine Research, 27570 Bremerhaven, Germany; thomas.soltwedel@awi.de

[5] Arctic Geophysics Department, UNIS—The University Centre in Svalbard, P.O. Box 156, N-9171 Longyearbyen, Norway; Ragnheid.Skogseth@unis.no (R.S.); Frank.Nilsen@unis.no (F.N.)

[6] Department of Marine Sciences, UGOT–University of Gothenburg, 100, SE-405 30 Gothenburg, Sweden; anna.wahlin@marine.gu.se

[7] CNR–ISAC—Italian National Research Council, Institute of Atmospheric Sciences and Climate, Bologna, I-40129, Italy; angelo.viola@artov.isac.cnr.it

[8] Department of Environmental Sciences, Informatics and Statistics, DAIS—University Ca' Foscari of Venice, 30172 Mestre, Italy; rubino@unive.it

* Correspondence: mbensi@inogs.it; Tel.: +39-040-2140431

check for updates

Abstract: Water mass generation and mixing in the eastern Fram Strait are strongly influenced by the interaction between Atlantic and Arctic waters and by the local atmospheric forcing, which produce dense water that substantially contributes to maintaining the global thermohaline circulation. The West Spitsbergen margin is an ideal area to study such processes. Hence, in order to investigate the deep flow variability on short-term, seasonal, and multiannual timescales, two moorings were deployed at ~1040 m depth on the southwest Spitsbergen continental slope. We present and discuss time series data collected between June 2014 and June 2016. They reveal thermohaline and current fluctuations that were largest from October to April, when the deep layer, typically occupied by Norwegian Sea Deep Water, was perturbed by sporadic intrusions of warmer, saltier, and less dense water. Surprisingly, the observed anomalies occurred quasi-simultaneously at both sites, despite their distance (~170 km). We argue that these anomalies may arise mainly by the effect of topographically trapped waves excited and modulated by atmospheric forcing. Propagation of internal waves causes a change in the vertical distribution of the Atlantic water, which can reach deep layers. During such events, strong currents typically precede thermohaline variations without significant changes in turbidity. However, turbidity increases during April–June in concomitance with enhanced downslope currents. Since prolonged injections of warm water within the deep layer could lead to a progressive reduction of the density of the abyssal water moving toward the Arctic Ocean, understanding the interplay between shelf, slope, and deep waters along the west Spitsbergen margin could be crucial for making projections on future changes in the global thermohaline circulation.

1. Introduction

Water masses in the eastern Fram Strait, strongly influenced by the interaction between Atlantic and Arctic waters and by local atmospheric forcing, substantially contribute to drive the global thermohaline circulation [1–4]. There is a remarkable variability in the system due to several forcing mechanisms (e.g., atmospheric, internal, tidal, shelf dynamics) that play an important role, especially in the upper layer [5–10]. On the contrary, it is not completely clear which processes are responsible for the inter-annual and seasonal deep flow variability in the western offshore Spitsbergen region [11,12]. Several studies, using both experimental and numerical modelling approaches, have addressed the role of interactions between Atlantic Water (AW) carried by the West Spitsbergen Current (WSC, [10,11,13–16]), and shelf and fjord waters [2,17–20] in the observed variability. Some of the processes that may be relevant for deep water circulation and variability in the western Spitsbergen region have been summarized in Figure 1.
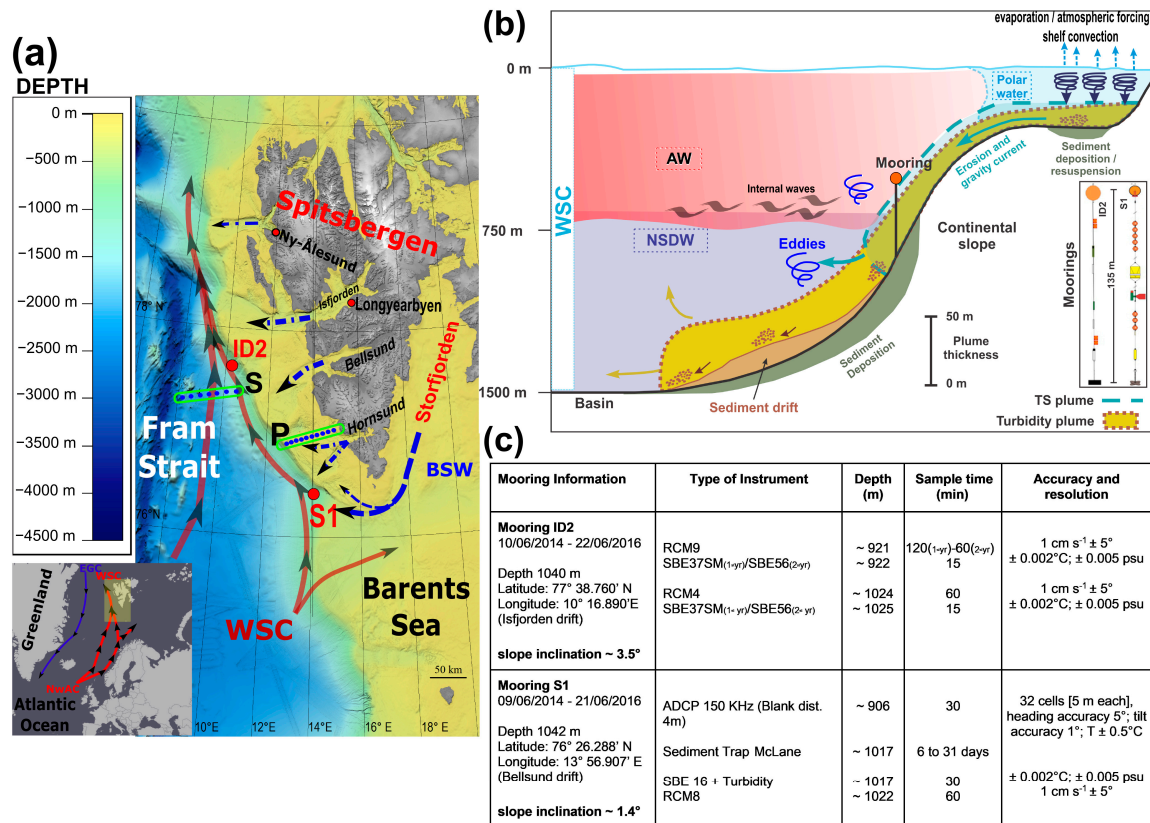

Figure 1. (**a**) Map of the study region showing bathymetry and main currents in the Fram Strait and along the west Spitsbergen margin. Red dots indicate the location of moorings S1 and ID2. Blue dots indicate CTD (conductivity-temperature-depth) stations along transects S and P. (**b**) Schematic of the shelf-slope dynamics along the west Spitsbergen slope (figure modified from [6], © American Meteorological Society. Used with permission). (**c**) S1 and ID2 moorings configuration and specification of instruments. (AW = Atlantic Water; NSDW = Norwegian Sea Deep Water; WSC = West Spitsbergen Current; BSW = Brine-enriched Shelf Water; EGC = East Greenland Current; NwAC = Norwegian Atlantic Current).

With this study, we aim at exploring signals observed in time series of temperature, salinity, current velocity, and turbidity, acquired by two near-bottom moorings (S1, ID2; Figure 1) deployed to assess the deep flow variability on short-term, seasonal, and multi-annual time scales in the southwest region offshore the Spitsbergen margin [12]. We also discuss potential links between the local oceanographic and atmospheric forcing in regulating shelf/deep sea interactions, which in turn can trigger baroclinic (internal) waves that stimulate internal mixing in the ocean (Figure 1b). Finally, we put the observed variability in the context of larger-scale circulation changes.

The overall circulation in the eastern Fram Strait (Figure 1) includes the northward flow of the WSC, i.e., the northernmost extension of the Norwegian Atlantic Current [21,22]. Flowing at a steady pace of about 0.25 m s^{-1}, following the 1000-m isobath [23], the WSC transports warm and saline AW into the central Arctic Ocean and, beneath it, colder and fresher Norwegian Sea Deep Water (NSDW, [15,24]) that occupies the deep local layer (Figure 1b). The NSDW is influenced by water contributions from the Greenland Sea (south of Fram Strait) and Eurasian Basin (north of Fram Strait, [15,24]).

Shoreward of the WSC, the Spitsbergen continental shelf is influenced by Arctic waters as well as by drifting sea ice [19]. The northward WSC is compensated by the southward East Greenland Current, which transports cold and fresh Polar Water across the western part of the Fram Strait. The WSC is topographically steered along the continental slope [2,25] with streamlines parallel to contours of constant f/H (Coriolis parameter/water column thickness). It has been traditionally considered as a barotropic flow [13,21]. However, more recent studies have outlined its baroclinic component, together with associated instabilities and eddy formations [14,26]. The AW occupies a large portion of the water column within the WSC (roughly between the surface and 600 m depth; [10]) and its properties undergo a strong interannual variability [27].

Relatively warm and cold periods of AW have been alternating in the last century: cold periods took place during 1900–1920 and 1955–1985, while a warm period occurred in the 1930s–1940s [27]. More recently, two warm AW anomalies passing through the Fram Strait occurred in 1999–2000 and 2005–2007 [22]. Temperature increase (0.06 °C year^{-1}, [22]) was accompanied by salinity increase (0.003 year^{-1}, [28]). However, based on monthly gridded fields of the meridional current component, no significant trend in the volume transport of AW was observed [22]. A warming of the Arctic Ocean, recorded since 1985 [27,29] became particularly evident in the WSC core after 2004, along with an intensification of the northward propagation of the AW warm signal [30]. Concomitantly with this evolution, the AW influence on temperature and salinity on the West Spitsbergen Shelf and in fjords of the Archipelago (e.g., Hornsund and Kongsfjorden, [20,31]) has become stronger in the last years, probably due to changes in the patterns of the dominating large atmospheric pressure fields [2]. It is not entirely clear to what extent the increased heat transport toward the Arctic is related to a strengthening of the Atlantic Meridional Overturning Circulation [32], to an increase in temperature or in volume of the AW [4,33], or, instead, to the variability of the AW transport along the two preferential pathways (Barents Sea and Fram Strait branches, [33]). Notably, the AW heat transport [29,34] can affect air temperature especially during winter [35], which in turn has direct effects on the dense water formation around the Spitsbergen margin.

In the west Spitsbergen region ocean-atmosphere interactions lead to multiple oceanographic processes, like shelf-slope dynamics, deep water variability through Polar and Atlantic waters interaction, as well as sea ice and dense water formation [1–3,7]. Dense water formation off the southwestern tip of Spitsbergen and in the Fram Strait depends on the rate of cooling (heat loss to the atmosphere) and homogenisation of the upper layers (i.e., water column stratification and mixing depth), sea ice growth, and brine rejection. Brine-enriched Shelf Waters (BSWs) are formed during ice formation in coastal polynyas [36–40]. Within fjords, and in particular in Storfjorden (the largest fjord in the Svalbard Archipelago, see Figure 1a) the accumulated water close to the freezing point has salinity ranging typically between 34.8 and 35.8 [38]. A 120 m deep sill separates this fjord from the shelf edge, and dense water overspills the fjord with strong inter-annual variability [38]. Eventually, it flows northwards along the shelf and the continental slope west of Spitsbergen, at depths where

water of similar density is transported by the WSC [41,42]. Numerical models [17,42] simulated the evolution in time and space of the plume in this region, revealing that it can reach velocities as high as 0.6 m s^{-1} over the continental slope.

Dense water spreading is also strongly influenced by tidally induced dispersion [8,9] and by bathymetric constraints [43]. Tides can drive barotropic and baroclinic water exchanges [44], and also generate shelf waves, which propagate as topographically trapped internal waves [13,45] stimulating mixing in the ocean interior. Inall et al. [44] reported about coastal trapped waves in Kongsfjorden, a western Spitsbergen fjord at latitudes (79° N) where the internal Rossby radius is small and the effects of trapped waves become more evident. Increased bottom shear velocities caused by the interaction of semidiurnal internal tides with the sloping bottom can cause sediment resuspension and prevent deposition, shaping thus the continental slope [46]. Topographically induced intrusions are also responsible for the generation of nepheloid layers (i.e., turbid layers with significant amounts of suspended sediment) transported along isopycnals [16,47]. Numerical models support geological observations showing that suspended sediment transported by bottom-arrested gravity plumes may have a role in the slope convection, by increasing the kinetic energy and the bulk density of the water (Figure 1b, [5,6]). Along their routes toward the abyss, offshore southwestern Svalbard, temperature of water plumes increases, while salinity decreases rather slowly due to entrainment of surrounding warm, but relatively saline AW [41,42,48,49]. The mixing and entrainment of these plumes with AW can reduce the maximum reached depth during their cascading [10,17,41,48]. According to Akimova et al. [48], BSW plumes leaving Storfjorden reached the bottom of the Fram Strait only three times, in 1986, 1988, and 2002, over a period from 1984 to 2003. Eddies can also break away from density-driven currents, as demonstrated in laboratory experiments and numerical models [42,50]. Intruding dense water can generate cyclones in the water above and anticyclones in the water below the depth of intrusion [43].

2. Data and Methods

2.1. Oceanographic Moorings

Various instruments attached to two oceanographic moorings (S1, ID2; Figure 1) collected data within a ~150 m thick near-bottom layer along the west Spitsbergen continental slope from June 2014 until June 2016. The payload of mooring S1 included a downward looking ADCP (Acoustic Doppler Current Profiler, Teledyne RD Instruments, Poway, CA, USA) RDI 150 kHz located ~140 m above the sea bottom, a CTD (Conductivity-Temperature-Depth) SBE16 (Sea-Bird Electronics, Bellevue, WA, USA) with Seapoint turbidity meter (Seapoint Sensors, Inc., Exeter, NH, USA) coupled with a sediment trap McLane (PARFLUX Mark 78H-21, McLane Res. Labs, East Falmouth, MA, USA) ~25 m above the sea bottom, and a single point Aanderaa current meter (Aanderaa Data Instruments, Bergen, Norway) RCM8 ~20 m above the sea bottom. Turbidity expressed as Formazin Turbidity Unit (FTU) was calibrated in the laboratory to obtain the corresponding values of suspended sediment concentration (mg L^{-1}). Mooring ID2 was equipped with two Aanderaa current meters (RCM9 and RCM4, ~120 m and ~20 m above the sea bottom, respectively) and two CT SBE37-MicroCAT recorders below each current meter (substituted with T loggers SBE56 in June 2015). A complete scheme of each mooring line (position, bottom depth, instrument type, deployment depth, and sampling time interval) is presented in Figure 1c.

The recorded data were post-processed after each recovery (June 2015, June 2016). Data with different sampling frequencies (15 min, 30 min, or 120 min) were averaged or interpolated to obtain homogenous hourly time series. Temperature, salinity, and turbidity data have been cleaned and despiked according to MyOcean in situ quality control standards and methodology (http://catalogue.myocean.eu.org/static/resources/user_manual/myocean/QUID_ INSITU_TS_OBSERVATIONS-v1.0.pdf). Moreover, temperature and salinity time series were checked by comparing them with data from CTD casts performed before and after each mooring deployment.

Potential temperature (θ), salinity (S), and potential density anomaly (σ$_\theta$) were calculated from in situ data. Note that only in situ temperature was recorded at ID2 between June 2015 and 2016, when thermistors (without conductivity sensors) were used, hence it was not possible to obtain θ, S, and σ$_\theta$.

Each vertical cell of the ADCP was treated as an individual time series. Current vectors, both from ADCP and RCMs, were decomposed into u (eastward, zonal), v (northward, meridional), and w (vertical) components. Tidal constituents, obtained from harmonic analysis with a signal-to-noise ratio > 1, were subtracted from the original time series, to provide de-tided data [51]. For specific analyses, a low-pass filter with a cut-off period of 33 h was applied to the de-tided time series to remove inertial oscillations and obtain sub-inertial non-tidal flow (i.e., sub-tidal). The principal component analysis was applied to the time series to determine the direction of the major variance of the deep currents. As this direction almost coincided with the along-slope component, the coordinate system was rotated accordingly. The angles of rotation in the trigonometric system were between −34° and −52° at S1, and between −40° and −48° at ID2. By rotating the reference system two new components for the velocity, i.e., *ur* (along-slope) positive towards SE, and *vr* (cross-slope) positive towards NE, were obtained.

Correlation and cross-correlation coefficients calculated between different variables, and reported further in the text, are always within the significance level of 0.05, unless otherwise specified.

2.2. Oceanographic Surveys

CTD measurements during oceanographic cruises provided vertical profiles of temperature (T) and conductivity (C) approaching the seabed within ~ 7–10 m. θ, S, and σ$_\theta$ were calculated from in situ data using MATLAB toolbox TEOS-10 (Gibbs SeaWater Oceanographic Toolbox) including thermodynamic equations of seawater (http://www.teos-10.org/software.htm). Oxygen concentrations were measured using a SBE43 sensor mounted on the CTD/Rosette Water Sampler while taking water samples at discrete depths for Winkler titrations [52]. Data were quality checked and averaged every 1 dbar with overall accuracies within ± 0.002 °C for T, ± 0.005 for S, and 2% of saturation for oxygen. Turbidity in the water column was detected by optical sensors mounted on the CTD probe.

CTD data used in this study come from the PREPARED cruise (r/v G.O. Sars, June 2014, PREsent and PAst flow REgime on contourite Drifts west of Spitsbergen), HH cruise (r/v Helmer Hanssen, June 2015), PS99.1 cruise (I/B Polastern, June 2016), and from oceanographic cruises carried out by the University Centre of Svalbard (UNIS) between 2014 and 2016 along section P (Figure 1). Long-term (1997–2017) yearly variability and linear trends were calculated from hydrographic data collected during AREX cruises carried out by the Institute of Oceanology Polish Academy of Sciences (IOPAN, [28]). In our study, we consider data collected along section S (~ 77°30′ N, see Figure 1) in the proximity of mooring ID2, from which we calculated the yearly values of θ, S, and σ$_\theta$ averaged in the upper-intermediate (100–800 m depth) and in the deep layers (>800 m depth). Trends have been calculated using a linear regression model (Table 1). Standard error (SE) and Root Mean Squared Error (RMSE) for each statistically significant (p < 0.05) trend are also reported in Table 1. In order to focus on the variability of the AW in the upper layer, we only take into consideration CTD measurements that have temperatures compatible with those of the AW (i.e., θ > 2°) in addition to the depth criterion [22]. Furthermore, we use the thickness of the AW layer as the weight while calculating the average θ, S, and σ$_\theta$ values. Some figures presented in this paper were elaborated using the Ocean Data View software [53].

Table 1. Linear trends of θ, S and σ_θ in the intermediate (100–800 m) and deep (>800 m) layers from CTD casts collected along section S (see Figure 1 and Figure 3). Data cover the period from 1997 until 2017. Significant linear trends (p < 0.05) are reported in red.

	Metrics	Layer 100–800 m and θ > 2 °C Criterion	Layer > 800 m	Layer > 800 m Sub-Period 2009–17
θ	Trend (°C)/year ± SE	0.0314 ± 0.0121	0.009 ± 0.0016	0.0222 ± 0.0033
	RMSE	0.3362	0.0445	0.0254
	p-value	0.01779	0.00002	0.00026
S	Trend /year ± SE	0.0042 ± 0.0007	0.0005 ± 0.0001	0.0007 ± 0.0002
	RMSE	0.0202	0.0035	0.0013
	p-value	0.00001	0.00083	0.00399
σ_θ	Trend (kg m^{-3})/year ± SE	0.0004 ± 0.0010	0 ± 0.0001	−0.0004 ± 0.0001
	RMSE	0.0272	0.0036	0.001
	p-value	0.69369	0.89612	0.01304

2.3. Atmospheric Data

To study atmosphere-ocean interactions between 2014 and 2016 we employed ERA-Interim dataset from the ECMWF (European Center for Medium-Range Weather Forecasts interim reanalysis) regularly spaced at 0.75° (interpolated at 0.25°) of latitude and longitude and available at 6 h time intervals. We initially compared the ECMWF output (e.g., wind speed/direction, air temperature) with data collected at the Amundsen-Nobile Climate Change Tower (CCT, see http://www.isac.cnr.it/~{}radiclim/CCTower/) in Ny-Ålesund. The 34 m high tower is equipped with a large set of instruments along the vertical to investigate physical properties of the atmospheric boundary layer over a long period and to study the turbulent exchange processes of energy and mass at the atmosphere-land interface. The comparison between land observations of wind speed and direction and ECMWF data revealed that both short-term and seasonal variabilities recorded at the CCT are reproduced coherently at S1 and ID2 locations (not shown). Hence, six meteorological parameters were selected from ECMWF dataset to characterize the air-sea interface: air pressure at sea-level, total cloud cover, 10 m zonal (*u*) and meridional (*v*) wind components, 2 m air and dew point temperatures, and sea surface skin temperature. The total heat flux (daily and monthly mean values) at the air-sea interface was computed taking into account four heat flux components also downloaded from ECMWF dataset: solar radiation, net longwave radiation, latent and sensible heat. The heat loss and the relative sea water temperature variation occurring during winter months were estimated using the methodological approach described in [54]. To analyse the periodicity and recurrence of intensive events, a Morlet wavelet analysis [55] was applied on the horizontal principal components both of the ECMWF wind data and of the current velocity at moorings S1 and ID2. The obtained results enabled studying non-stationary signals and investigating the dynamic response of the marine currents to the atmospheric forcing.

3. Results

3.1. Thermohaline Patterns on the West Spitsbergen Margin during Oceanographic Cruises between 2014 and 2016

Vertical distribution of hydrographic data along the zonal section P (Figure 1) on the West Spitsbergen Shelf north of Hornsund is shown in Figure 2. It refers to data collected in April 2014, June 2014, May 2015, and August 2016. Thermohaline properties on the shelf, usually occupied by Arctic Water [2,56], show a large seasonal and interannual variability. They depend on the variability of waters transported by the coastal current itself, on the seasonal variability in the contribution of fresh water from the main fjords, and on the variability of the AW inflow from offshore, whose properties and extension vary with large-scale circulation patterns in the area.
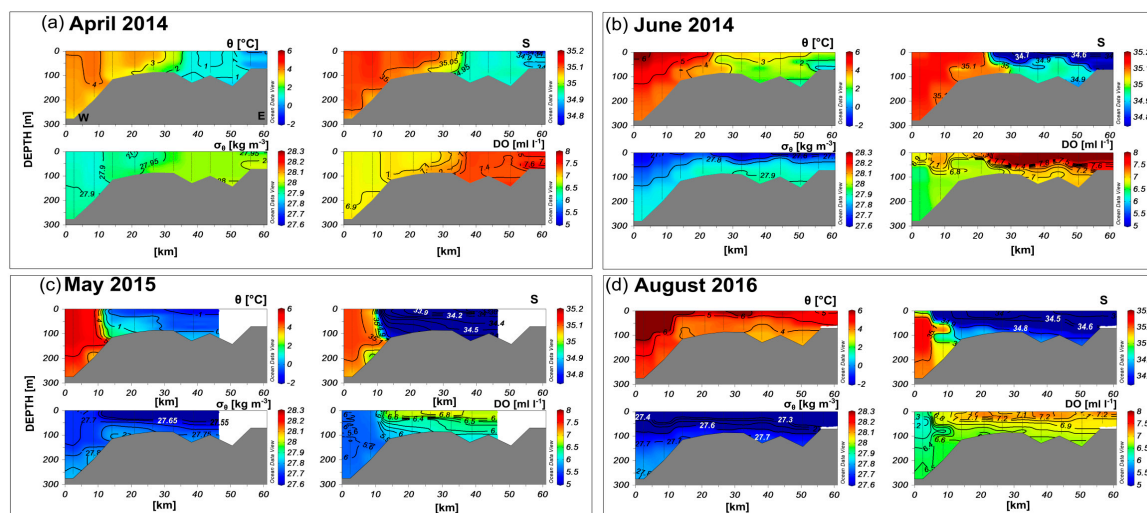
Figure 2. θ (°C), S, σ_θ (kg m^{-3}), DO (mL L^{-1}), along the W–E section P (see Figure 1) in April 2014 (**a**), June 2014 (**b**), May 2015 (**c**), and August 2016 (**d**) on the West Spitsbergen Shelf area. The data are from the PREPARED cruise and from several UNIS cruises.

In April 2014 (Figure 2a), the westernmost part of the section was occupied by warm and saline AW (3°C < θ < 4°C and S > 34.9), while its easternmost part was filled by cool and fresh water (θ < 1 °C and S < 34.9). AW could also be detected by its lower oxygen content with respect to Arctic Water. In June 2014 (Figure 2b), during the PREPARED cruise, a cold and fresh waterfront extended offshore. At that time, the westernmost part of the shelf was occupied by AW. The latter was also present on the continental slope, roughly down to 800 m depth, above the NSDW in the deep layer (>800 m, not shown). At depths between 100 m and 800 m, where AW was present, values of θ ~ 0–4.5°C, S ~ 34.95–35.1, σ_θ ~ 27.85–28.05 kg m^{-3}, and dissolved oxygen (DO) ~ 6.4–6.6 mL L^{-1} were found, while at depths larger than 800 m θ was below 0 °C, S ~ 34.91, σ_θ ~ 28.05–28.08 kg m^{-3}, and DO ~ 6.2–6.4 mL L^{-1}. Light transmission (not shown) decreased when approaching the seabed, revealing high suspended matter concentrations in the bottom layer of the shelf and continental slope. In May 2015, AW retreated offshore (Figure 2c) like in August 2016 (Figure 2d) when, however, θ was everywhere larger than 3 °C and S values were relatively low (<34.85) in the shallow part of the section. In August 2016, the AW was confined in the western part of the section and it was characterized by the highest θ and S values (θ > 6 °C and S > 35.15). Overall, a large variability characterizes the temporal and spatial evolution of the observed parameters along the section [2]. In some cases sharp thermal and saline fronts tend to compensate, and no density structure was found (Figure 2b,c).

3.2. Multiannual Variability of the Thermohaline Properties along the West Spitsbergen Margin

CTD casts carried out during annual IOPAN summer cruises aboard the r/v Oceania between 1997 and 2017 help to understand the interannual variability of the thermohaline properties of the along-slope flow (i.e., WSC). Data collected yearly along section S (Figure 1) at latitude ~ 77°30′ N, close to the ID2 mooring, were spatially averaged within two layers: the upper-intermediate layer, between 100 and 800 m, where the AW is detected by the additional θ > 2 °C criterion, and the deep layer (>800 m), mainly occupied by NSDW (Figure 3). Linear trends were calculated for each of the three variables, θ, S and σ_θ (Table 1). They revealed long-term positive trends of θ and S in the upper layer, while no significant trend was found in the σ_θ (Figure 3). However, the upper layer went through relatively warm and saline periods (i.e., 2005–06 and 2011–12) as well as cold and fresher periods (i.e., 2003–04, 2008, and 2013). Noteworthy, starting from 2013 an overall θ increase was not accompanied by S increase. In the deep layer, slightly positive long-term trends in θ and S were also found, and they became more evident between 2009 and 2017, when also a small but significant trend in σ_θ decrease was detected. Years characterized by higher standard deviations for S in the deep layer (i.e., 2000,

2002, 2006, 2008) may indicate the occurrence of advection/intrusion phenomena of different water masses into the layer. No significant correlations ($p < 0.05$) were obtained by comparing detrended time series between the upper and deep layers for each parameter. Observed trends are in agreement with results published by, e.g., Chatterjee et al. [57], where authors point out how changes in the AW properties depend on the strength of the subpolar gyre in the North Atlantic, which in turn is strongly influenced by the wind stress curl. The analysis of the multi-annual variability of the average thermohaline properties gives a general framework in which we undertake a more detailed deep flow variability analysis (including high-frequency signals) presented in the following section. The trends exposed here also provide an indication that the abyssal layer west of Svalbard is slowly becoming warmer and saltier on long temporal scale.
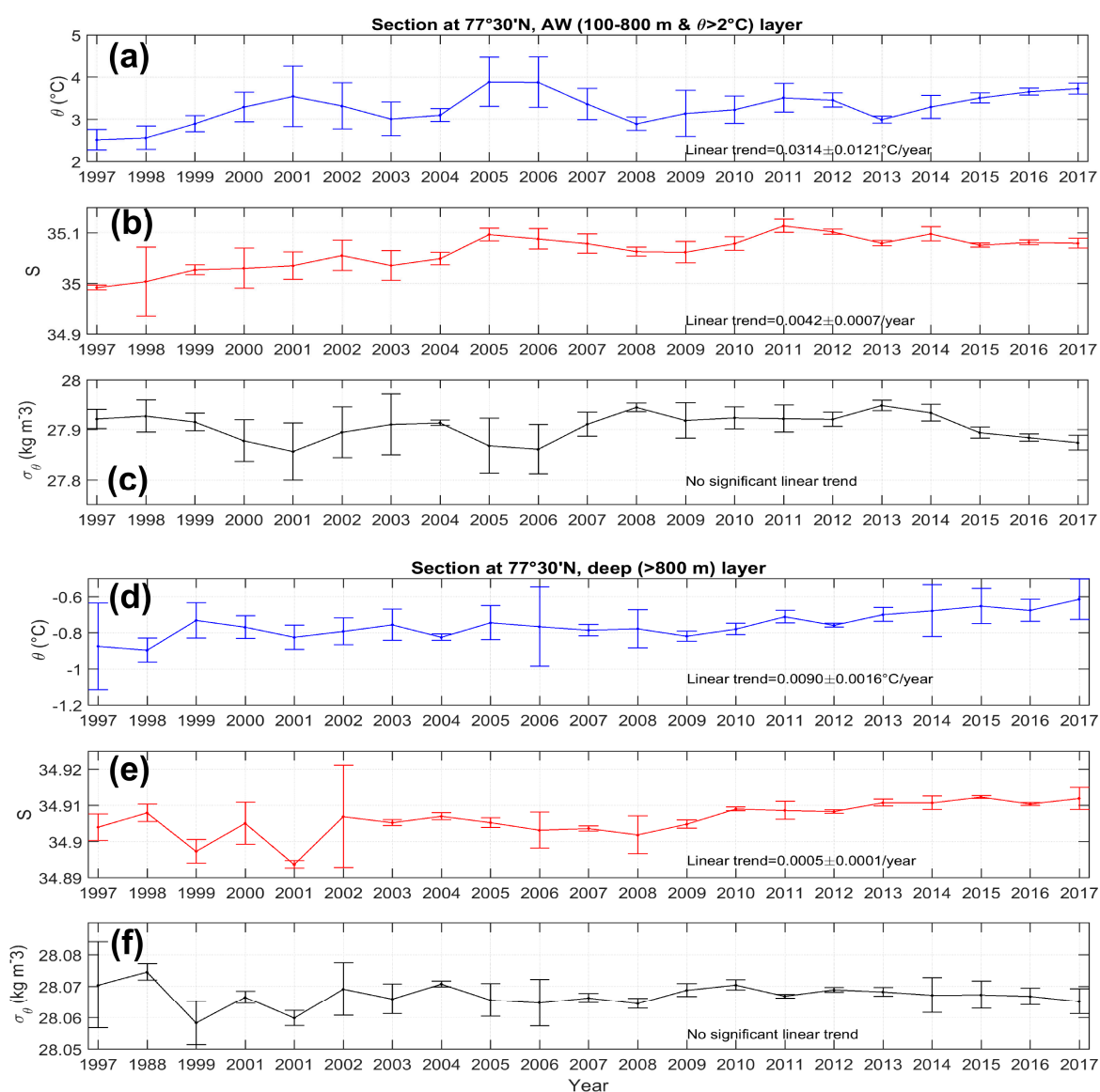

Figure 3. Weighted average of thermohaline properties (θ, S, σ_θ) calculated from CTD stations along the section S at ~ 77°30′ N (between 8 and 10°30′ E, see Figure 1): upper layer (**a**–**c**) (100–800 m with θ > 2 °C) and deep layer (**d**–**f**) (>800 m). Weights are defined by the layer thickness at each station where bottom depth varied between 1000 and 2300 m. Data are from the hydrographic measurements carried out during summer AREX cruises aboard r/v OCEANIA (IOPAN).

3.3. Temporal Variability in Oceanographic Parameters at Moorings S1 and ID2

Time series data recorded at moorings S1 and ID2, at depths >900 m, highlighted the presence of water with properties ($\theta \sim -0.90\,°C$, S $\sim$ 34.91, and $\sigma_\theta \sim 28.07\,kg\,m^{-3}$) typical of the NSDW [46]. However, perturbations caused by occasional "thermohaline intrusions" of water, which is warmer (up to ~2 °C), saltier (up to ~35), and less dense (down to 27.98 kg m^{-3}), are evident in Figures 4 and 5. Noteworthy, temporal fluctuations of θ, S, and σ_θ were particularly apparent between October and April and occurred almost simultaneously at both moorings, ~170 km apart from each other (see Figure 1a). A larger variability was recorded during winter 2014–15 at both sites. The duration of the observed intrusions of relatively warm and salty water varied from a few hours to several days (up to 10–15 days), during which thermohaline variations oscillated mainly at a diurnal (24 h) frequency.
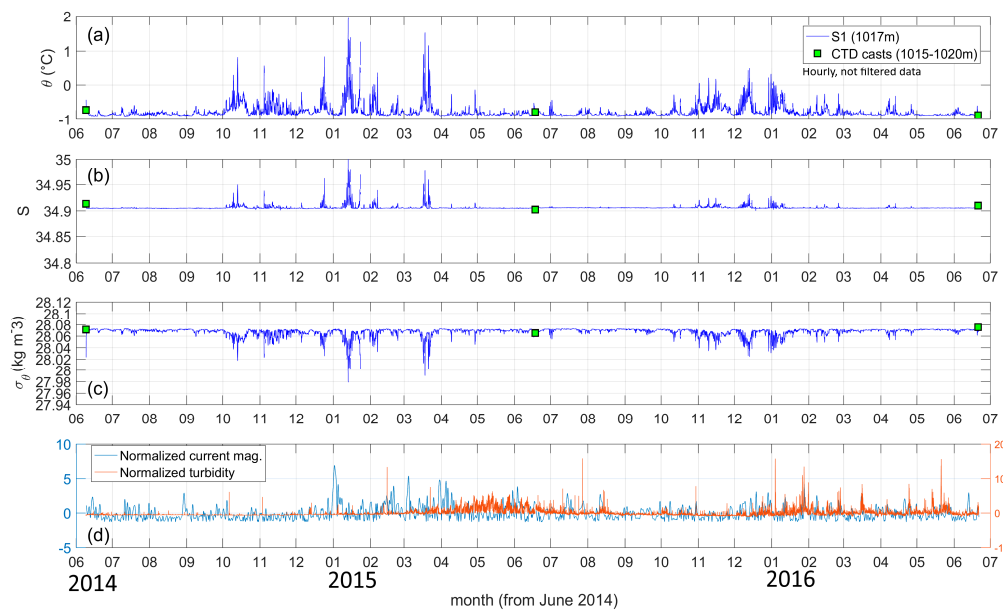

Figure 4. Time series (hourly data) of θ (**a**), S (**b**), and σ_θ (**c**) at S1 (1017 m depth). Green squares show data extracted from CTD casts (θ and S) at depths close to the moored instrument. Panel (**d**) shows normalized values of current magnitude (1022 m) and turbidity (1017 m). Data span from June 2014 to June 2016.

The normalized time series of current magnitude and turbidity at S1 are shown in Figure 4d (normalization was obtained by subtracting the average of each deployment phase and dividing by the corresponding standard deviation). Turbidity peaks were observed generally from December to July. During the first year of measurements, high turbidity values were found around mid-May 2015, while in 2016 several episodes characterized by high turbidity were observed almost each month (Figure 4d).

Overall, data recorded at mooring ID2 show a larger variance with respect to S1 data, except for θ at 1025 m depth (Figure 5). During the first year of measurements, events associated with temperature increase occurred mainly between October and April (Figure 5), while during the second year they were limited to the period October–February (Figure 6).
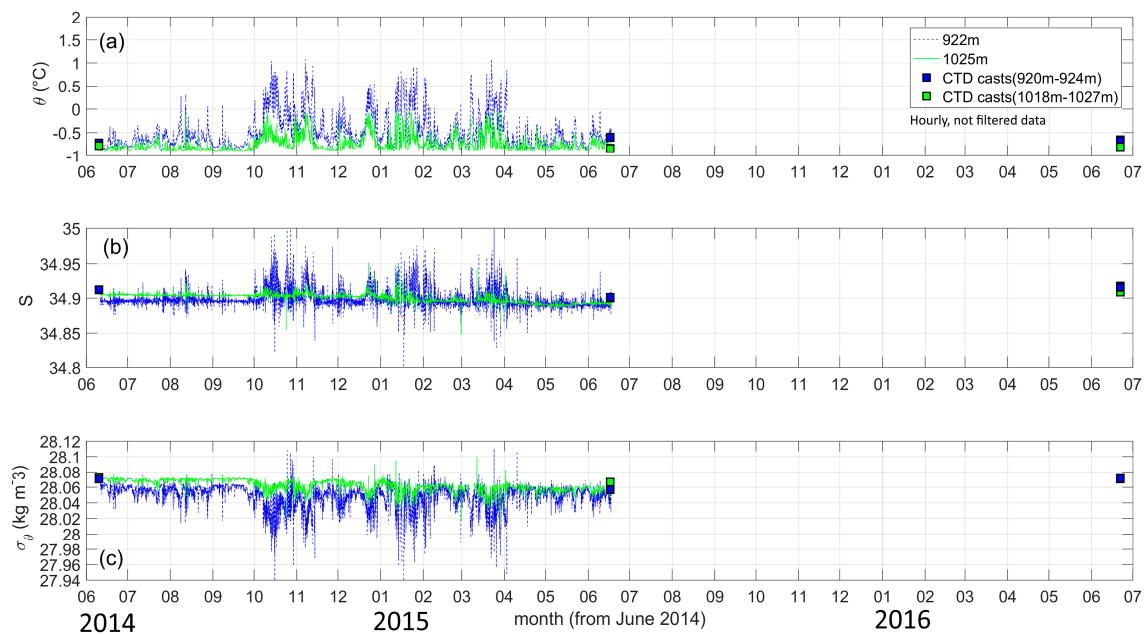
Figure 5. Time series (hourly data) of θ (**a**), S (**b**), and σθ (**c**) at ID2 between June 2014 and June 2015 at 922 m and 1025 m depth. Green and blue squares indicate data extracted from CTD casts (θ and S) at depths close to the moored instruments. Note that after June 2015, only temperature sensors were deployed at ID2 (see in situ temperature in Figure 6).
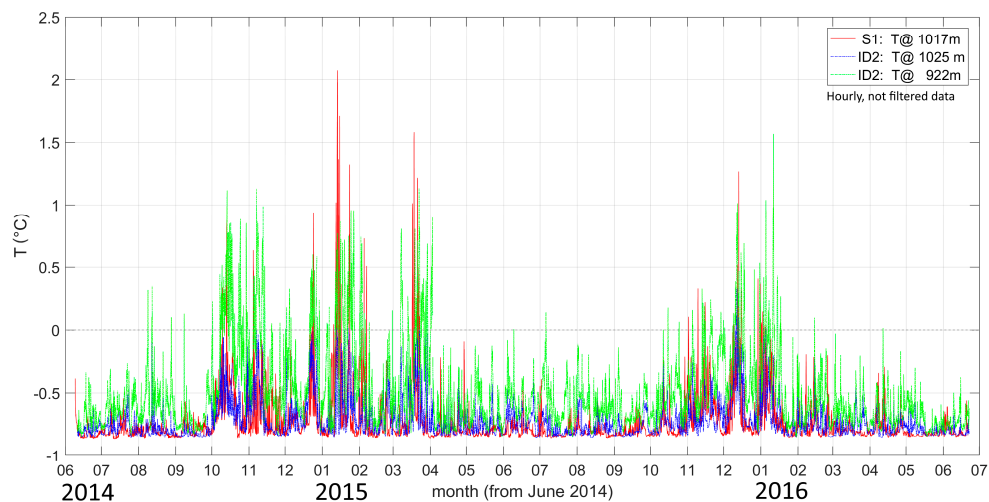

Figure 6. In situ temperature time series at S1 (red) and ID2 (blue and green). Data cover the period from June 2014 to June 2016 (for the position of the moorings refer to Figure 1).

The correlation between θ$_{ID2}$ at two depths (1025 m and 922 m) is rather high (0.75), while the correlation between S$_{ID2}$ at the two depths is smaller, 0.28. Short-term oscillations at 922 m were larger than at 1025 m (Figure 5). Moreover, the difference between S at 1025 m and S at 922 m diminished from ~0.01 to almost zero after one year. Accordingly, the difference in σθ progressively diminished as well (Figure 5c). This would be consistent with the effect of mixing in the ~100 m thick near-bottom layer.

A choice to bring together and compare the T (in situ temperature) time series at S1 and ID2 (Figure 6) rises from the fact that only temperature sensors were deployed at ID2 after June 2015. The lack of conductivity sensors prevented calculation of θ, S, and hence, of σθ as well. As said, T peaks appeared almost concomitant at the two stations. A significant cross-correlation, ~0.43–0.45, between T recorded at S1 and ID2 was found with the maximum value corresponding to a time lag of

5 h. Similarly, but not shown in Figure 6, S peaks were almost simultaneous at the two stations, despite small cross-correlations (0.06 between S1 and ID2 at 1025 m; 0.17 between S1 and ID2 at 922 m).

In general, large current velocities were observed during the winter period. To study more in detail the possible linkage between the ocean currents and the thermohaline variability in the deep layers at S1 and ID2, we focus on the most energetic period, 1 October 2014–30 April 2015 (Figure 7). A similar variability (but less energetic) was observed also in the period October 2015–April 2016.
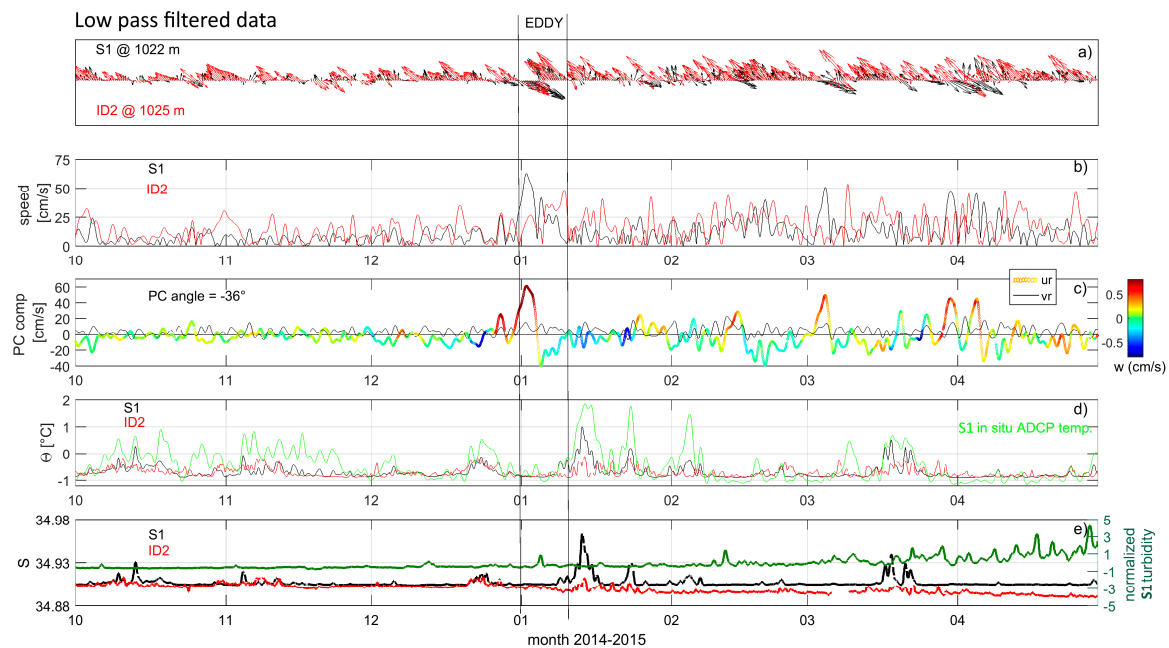

Figure 7. Time series at S1 and ID2. (**a**) Stick diagram of deep currents; (**b**) current magnitude; (**c**) current component along the direction of maximum variance at S1 (1017 m depth, *ur* positive towards SE); the colorbar refers to vertical velocity (*w*) from the ADCP at the same depth. The angle of maximum variance is referred to the trigonometric system; (**d**,**e**) θ and S at 1017 m (S1) and 1025 m (ID2) depth. Temperature (T) from the ADCP at 909 m and turbidity are also shown (green lines in panels d and e). Data refer to the period 1 October 2014–30 April 2015.

The principal components determined from current data revealed that the main direction of variability was along isobaths. In this frame, the appropriate velocity components are the along-slope (*ur*, positive towards SE) and the cross-slope one (*vr*, positive towards NE, i.e., toward the coast). Major events, mainly associated with anticlockwise (cyclonic) rotations, occurred at the beginning of January, beginning of March, and at the end of March 2015. They could be attributed to the passage of eddies at the mooring location. Sometimes these eddies were detected both at S1 and ID2, but with a certain time delay. This fact was particularly evident at the beginning of January 2015 (Figure 7a), when a cyclonic eddy lasted more than 10 days at S1, and it appeared at ID2 after approximately 30 hours. Strong (>40 cm s^{-1}) positive along-slope currents, and low (<10 cm s^{-1}) positive cross-slope currents (Figure 7c) characterized the first phase of this eddy passage, together with enhanced positive vertical velocities (upward). The second phase of the eddy passage was instead characterized by negative along-slope currents and slightly negative vertical velocities. In general, the eddy was not associated with significant θ and S variations. On the contrary, main episodic events with enhanced θ and S values (Figure 7d,e) were associated with negative vertical velocity (i.e., downward flow, correlation was 0.13), but with relatively small horizontal velocities (Figure 7b–d). Such episodic increases in θ and S seem to occur coherently throughout the 100 m thick bottom layer. The correlation between *ur* (*vr*) and θ was small and around −0.14 (−0.14). However, the cross-correlation between θ and *vr* reached a maximum value (−0.27) with a time lag of 14 h (θ lags *vr*), probably suggesting that θ increases could be associated, to some extent and delayed in time, with enhanced negative cross-slope currents (i.e.,

directed offshore). It is noteworthy that the correlation between turbidity and *vr* (*ur*) at S1 was not statistically significant considering the period June 2014–June 2015, but it resulted significant, –0.41 (–0.13), by restricting the analysis to the period April–June 2015. These facts suggest that the seasonal increase of turbidity (Figure 4c) was mainly related to a major availability of sediment transported by cross-slope currents from the shelf to the deep sea during spring.

Progressive vector diagrams (Figure 8) show that sub-tidal currents at S1 were directed prevalently northwards, following, as expected, the bathymetric constraints. However, the prevalent current direction slightly changed with increasing depth: it tended to rotate clockwise approaching the seabed (Figure 8a). Periodical current reversals (with the current direction changing from NW to SE) were also evident with a periodicity of about 15 days, usually accompanied by stronger currents, especially during the winter season. Currents, in particular those at 1022 m depth (Figure 8b), were prevalently NE oriented between June 2014 and December 2015 (mean u = 0.5 cm s^{-1}, mean v = 4 cm s^{-1}), while they were prevalently NW oriented between January 2016 and June 2016 (mean u = −0.3 cm s^{-1}, mean v = 3.6 cm s^{-1}). In this last period, the prevalent direction of the flow resulted coherent throughout the deep layer at different depths (not shown) with only a very slight clockwise rotation with increasing depth. Moreover, less current reversals occurred, especially at the deepest measured level. This fact suggests the temporary presence of a more homogeneous deep flow during the last phase of measurements.
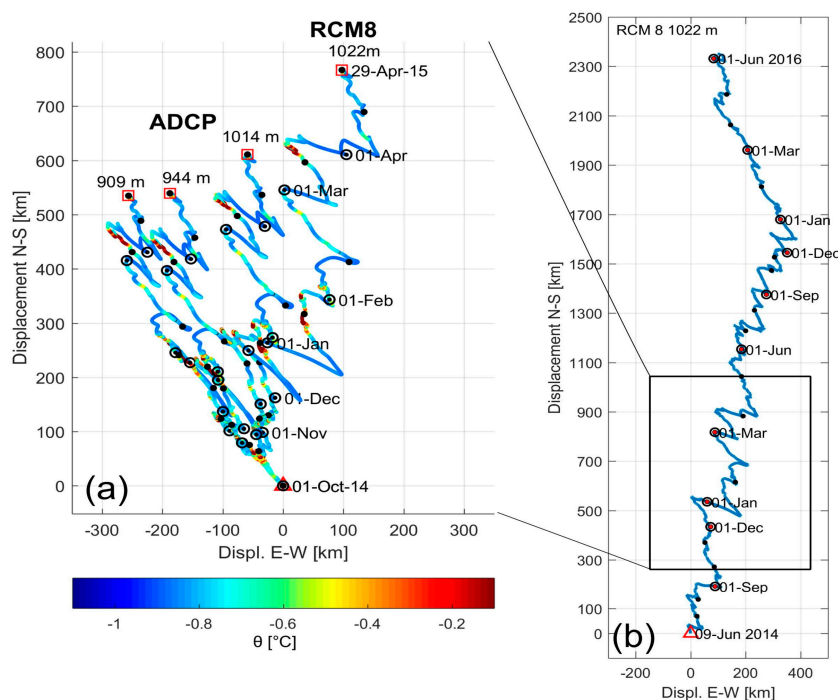

Figure 8. Progressive vector diagram of sub-tidal flow at S1. Panel (**a**): data from ADCP at different depths (909 m, 944 m, and 1014 m) and from current meter RCM8 at 1022 m within the period 1 October 2014–30 April 2015. The colorbar refers to θ at 1017 m depth. Panel (**b**): data from RCM8 at 1022 m within the whole 2-year period (June 2014–June 2016). Black dots correspond to the beginning of each month.

At ID2, the main direction of the sub-tidal currents followed the isobaths (not shown), like those observed at S1. It was prevalently northwestwards (mean u = −6.3 cm s^{-1}, mean v = 7.6 cm s^{-1} at 921 m, and mean u = −9.6 cm s^{-1}, mean v = 7 cm s^{-1} at 1024 m). The direction of the current changed slightly with increasing depth, but in the opposite way than at S1: indeed, while the main flow at 921 m depth was NW, it progressively became W–NW approaching the seabed, hence rotating anti-clockwise.

Moreover, from April 2016 to June 2016, at the deeper level (1024 m) the orientation of the main flow changed from NW to N–NE.

3.4. Local Wind Variability and Dynamic Response of the Ocean

To investigate the relation between atmospheric forcing and dynamic response of the deep layer, we compared the ECMWF time series with oceanographic data recorded at S1 and ID2. In general, in both years of measurements air temperature values decreased below 0 °C starting from September–October (Figure 9), with negative heat fluxes at the air-sea interface (heat loss from the ocean) until April. Maximum daily heat losses around −640 W m^{-2} occurred between December and March during intense storms characterized by strong (>10–15 m s^{-1}) northeasterly winds (not shown). Wintertime (December–March) monthly mean heat losses were between −200 and −260 W m^{-2}. Starting from May, most of the area southwest of Svalbard gained heat from the atmosphere (peak daily net heat flux values up to 200 W m^{-2}). Heat losses were larger during winter 2014–15 when a larger thermohaline and current variability at S1 and ID2 was observed as well, compared to the winter 2015–16. The correlation between ECMWF wind at S1 and ID2, using data smoothed with a daily moving average, is large (>0.84). It confirms the synopticity of meteorological events in the study region. Moreover, the correlation increases up to 0.91 using data smoothed with a seven-days moving average, which still reproduces accurately the features of the strongest events. Overall, by comparing ECMWF wind and currents at S1 and ID2 a coherent variability emerges (Figure 9). Indeed, we observed intensification of the deep currents during winter months when the wind was stronger. Cross-correlations revealed that current peaks lag those of wind by about one day at S1 (0.13), and two days at ID2 (0.08).
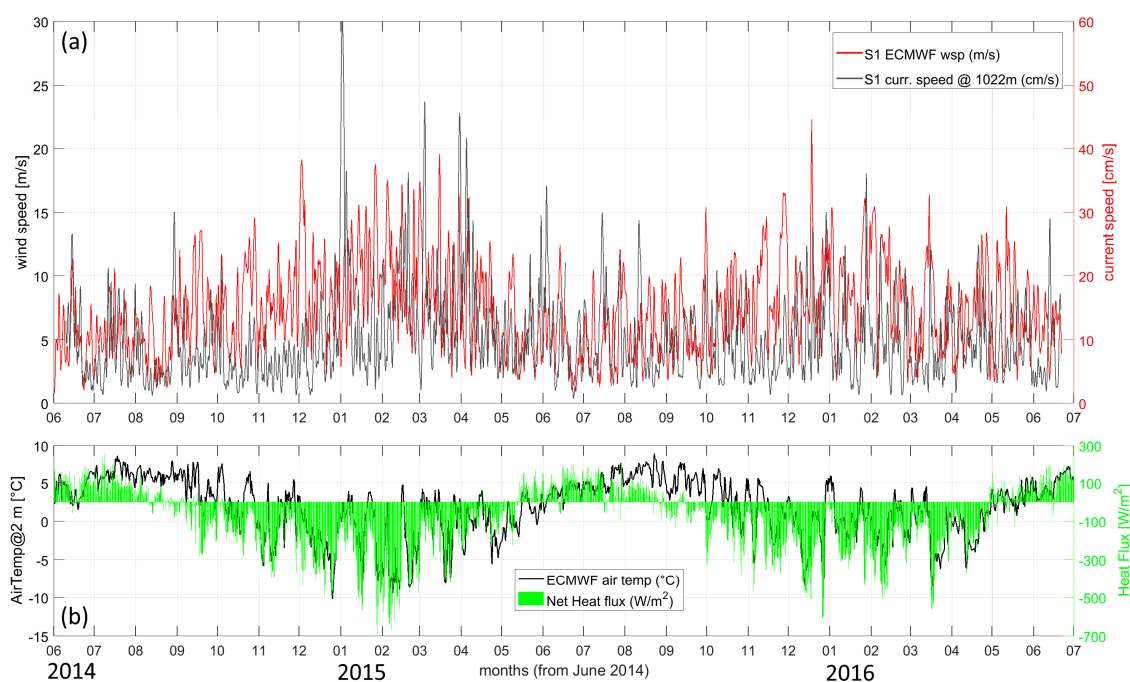

Figure 9. ECMWF wind speed (m s^{-1}) and deep current (cm s^{-1}) time series at S1 (**a**). Data are smoothed with a daily moving average. Air temperature (°C) and net heat fluxes (W m^{-2}) at the air-sea interface obtained from ECMWF ERA-Interim dataset (**b**).

In order to explore the temporal evolution of the energetic events at different time scales, the wavelet analysis was applied on the ECMWF wind and horizontal current decomposed into along-slope and cross-slope principal components. As far as the wind is concerned, there were no prominent differences between outcomes at the two mooring sites, hence, for simplicity, we present only results for S1. We found a pronounced intra-annual variation with the most energetic events occurring during winter months and characterized by periodicities around 500 h (~20 days). In general, the wind in

the summer period (i.e., June–August) was more quiescent (Figure 9) and the energy concentrated at a short time scale was much lower with respect to the energy concentrated at longer time scales (Figure 10e,f).
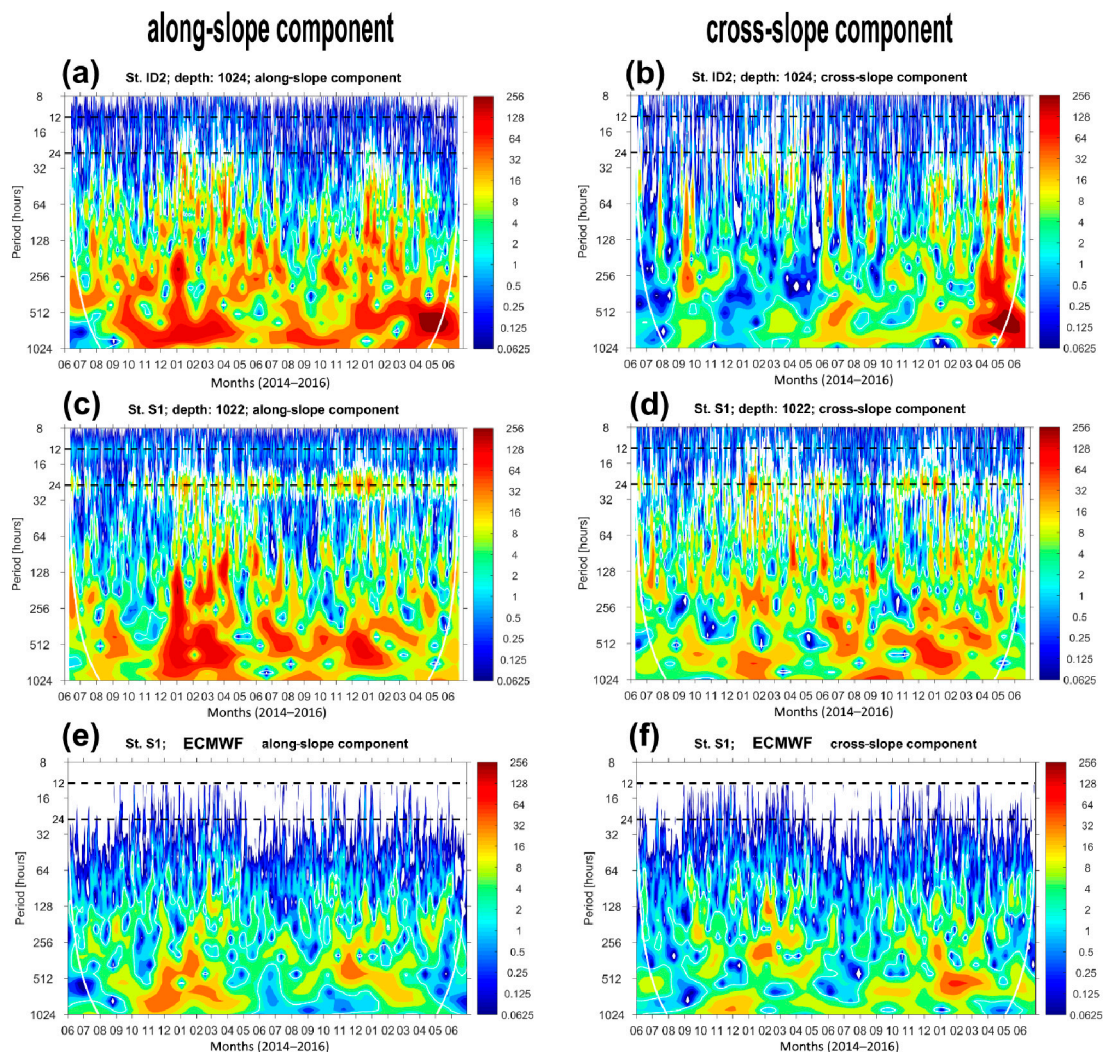

Figure 10. Wavelet power spectrum of the along-slope (**a,c,e**) and cross-slope (**b,d,f**) components (obtained from principal component analysis) of deep currents at ID2 and S1, and ECMWF wind data at S1 (not filtered). Periodicities of 12 and 24 h are indicated by black dashed lines.

The wavelet power spectrum of the horizontal currents at S1 and ID2 (Figure 10a–d) shows that the along-slope component was characterized by larger energy than the cross-slope one. However, the time evolution of the energetic events associated with the cross-slope current component (Figure 10b,d) reveals that major events at S1 occurred more or less regularly all over the study period, while at ID2 higher energy was found during the second year, with a peak between April and June 2016.

Referring to both components, most of the variance (i.e., kinetic energy) was concentrated in the low-frequency (long period) domain with typical periodicity centred around 500 h (~20 days) and ranging roughly between 200 and 1000 h (i.e., 1–6 weeks), similarly to what observed for the wind. Part of the energy was also distributed in the time domain between 50 and 200 h (i.e., 2–8 days), as well as in the high-frequency domain (~12, 24 h). As for the energy concentrated in the semidiurnal (12 h) and diurnal (24 h) time scales, which contain tidal signals, we found the former negligible compared to the latter. Noteworthy, the energy concentrated at the diurnal time scale was comparable for both components, although it was larger at S1 than at ID2, where it seems shifted to about 35 h. Moreover,

we found that the energy at the diurnal time scale in the cross-slope current component, in addition to being larger at S1 than at ID2, decreased with increasing depth (not shown). Another peculiarity of this signal is that it was not distributed regularly over time, contrary to what we may expect for tidally induced oscillations. In fact, there were periods of the year when the diurnal signal appeared more energetic, mostly during winter, while there were other periods (e.g., August–September 2014) when it was less pronounced or almost absent.

Summarizing, we found a correspondence between wind and current energetic events, especially at longer time scales. The energy induced by the wind and transferred to the water column can trigger fluctuations in the current field at different time scales, even at high frequencies. However, the fact that high energy over broad time scales appear also in periods when the wind is more quiescent, like during summer, suggests that the deep flow is influenced by various concomitant phenomena.

4. Discussion and Conclusions

Our measurements revealed the presence of vigorous deep current activity on the continental slope southwest of the Svalbard region. Several times, at depths of ~1000 m, we observed along-slope jets exceeding 40 cm s^{-1}, with highest values reaching ~60–70 cm s^{-1} (Figures 7 and 9). The prevalent flow was directed northward (from NE to NW), but periodical inversions of the flow were observed (Figure 8). In particular, the period December–March was the most energetic, as it was characterized by current magnitudes almost constantly larger than 30 cm s^{-1}. Thermohaline variations, with large peaks of temperature and salinity, were also observed mainly between October and April. They appeared almost concomitant at the two stations, which are ~170 km apart along the mean pathway of the WSC. In fact, the cross-correlation between temperature at S1 and ID2 revealed a time lag of about 5 h only. However, water parcels travelling with an average velocity of 30 cm s^{-1} would cover the distance between the two moorings in little more than one week. From our analyses, a strong eddy activity at both moorings was also evident. In particular, an energetic eddy that lasted more than 10 days at S1 in January 2015, was observed after about 30 h also at ID2 (Figure 7). Moreover, fluctuations of the thermohaline properties, as well as of the currents, included frequently diurnal time scale. According to these findings, we can exclude that such fluctuations observed at the two sites are part of localized phenomena transported along the west Spitsbergen slope by the WSC. In addition, we can exclude the presence of one large single eddy at both mooring locations since the typical diameter of mesoscale eddies in this polar region is around 10–20 km [58]. On the other hand, eddies may be a manifestation of the mesoscale variability that propagates along the shelf break and along the continental slope, and they are able to induce vertical water displacement. Similarly, the passage of trains of topographically trapped waves, with a predominantly diurnal periodicity, travelling along the continental slope may result in internal oscillations, highlighted by the observed thermohaline variability. This interpretation is in agreement with Nilsen et al. [45], whose findings revealed the presence of both mesoscale variability and topographically trapped waves at shallower depths (shelf break) in a wider zone including our study area, resulting from rotating wind field during passing storms. In particular, beside the mesoscale variability they found internal waves with wavelength λ = 32 km for periods of 24 h and 35 h. The passage of trains of internal waves would partly explain the thermohaline oscillations observed at the mooring sites since these waves can induce changes in the vertical distribution of the AW along the entire west Svalbard margin. A similar phenomenon was also observed in numerical simulations along the Norwegian continental shelf [59]. Lien et al. [59] found that general intensifications of North Atlantic Oscillation and consequent atmospheric events, are able to amplify the AW depth variability during winter, due to the Ekman cross-shore transport induced by the along-slope (i.e., along-shore) wind component. This fact seems in agreement with the enhanced winter energy found from the wavelet analysis applied to our data. Indeed, we found an overall consistency between the variability of the deep sea currents and the local wind signal (see Figure 9), especially on seasonal and low-frequency scales. In particular, we observed the occurrence of the most energetic events during winter both for the deep current flow and for the wind speed with typical

periodicities of ~20 days. Consequently, our interpretation is that the passage of high-low atmospheric pressure systems can explain the origins and amplification of internal oscillations observed along the west Spitsbergen margin at 1000 m depth. Meteorological forcing would hence modulate the current flow, extending its influence from the surface down to deep layers. Von Appen et al. [15] also found variability of deep ocean flows with periodicities of 1–3 weeks in the northern Fram Strait, at depths exceeding 2000 m. They explained such variability by the passage of basin-scale topographic Rossby waves excited by synoptic atmospheric forcing.

Sanchez-Vidal et al. [11] observed similar sporadic intrusions of relatively warm and salty water at their Stations A (close to S1) and B (1500 m depth, slightly deeper on the continental slope) in 2010–11. They suggested that such modifications of the ambient water at large depths were likely related to the influence of shallower AW. Moreover, they also found a 100 m thick bottom layer characterized by relatively high turbidity values, likely associable to a nepheloid layer. Increased turbidity along the west Spitsbergen continental slope can result from resuspension of sediment due to enhanced bottom currents (i.e., passage of trains of internal waves), but also from particles transported during cascading events, for example. According to this, we suppose that observed water intrusions at depths larger than 1000 m have two possible causes: (i) they originate from internal oscillations triggered by the passage of trains of internal waves or eddies, as discussed above; (ii) they occasionally originate from slope currents as a result of dense water formation and vertical mixing events occurring on the shelf, the latter being strongly influenced by the progressive intensification of the AW signal on the shelf and within fjords [20,31].

In support of the second hypothesis, we discuss here a combined analysis of meteorological and oceanographic data. Air-sea interaction and strong vorticity in the wind field lead to Ekman pumping and vertical convection over the West Spitsbergen Shelf [1,23,60]. Nilsen et al. [2] demonstrated that in the period autumn–winter (between September and May) low-pressure atmospheric systems influence the West Spitsbergen Shelf area. They also found a negative correlation with a zero time lag between along-shore wind stress and ocean temperature at their mooring I1, at the mouth of Isfjorden on the shelf, at 50 m and 190 m depths. Subsequently, northerly wind events (and associated positive wind stress curl field) could cause upwelling of AW that can be cooled after reaching the surface and become denser. The wintertime heat fluxes in our study had daily peak heat loss from the ocean to the atmosphere reaching −640 W m^{-2}, while average monthly in the period December–March had values around −200 W m^{-2}. Such heat losses could cool down by 2–3 °C the intruding warm and saline AW all the way to the bottom on the ~200 m deep continental shelf, in agreement with findings by Hakkinen and Cavalieri [61]. Cooling of this magnitude would increase the density of the AW (θ > 2 °C, S > 34.92, 27.70 <σ$_\theta$ < 27.97 kg m^{-3}) on the shelf by reaching values of ~28.04 kg m^{-3}, triggering the sinking of shelf water downslope to depths > 900 m (Figure 1b). Consequently, thermohaline and current variability observed in the deep layer at S1 and ID2 could also be sporadically caused by the arrival of gravity currents driven by dense water plumes formed over the shelf during intense meteorological events (i.e., those producing shelf convection) or formed after sea ice formation within fjords (i.e., BSW). Dense plumes descending as bottom-arrested currents follow preferential routes constrained by bathymetry, undergo a strong entrainment of AW that occupies the intermediate and upper layers of the WSC [41]. These dense plumes can collect sediments (Figure 1b) that increase their kinetic energy and bulk density [6,62,63]. In this regard, Fohrmann et al. [6] pointed out how a volumetric concentration of 1000 mg L^{-1} of suspended quartz particles increases the bulk water density of 0.6 kg m^{-3}. They also demonstrated how turbidity plumes in the Svalbard region are 10 times faster and can reach deeper layers with respect to mere temperature-salinity plumes. However, at S1, we found turbidity values up to 6 FTU in late winter season, corresponding to a concentration of suspended sediment of about 16–18 mg L^{-1}, which would not be sufficient to compensate the low density deriving solely from temperature and salinity. Hence, an input of sediments from the shelf/slope that would stimulate water cascading is plausible, but not so explicit from our data. In any case, at S1 we found a larger correlation between the cross-slope velocity component directed

offshore and turbidity during spring. This fact may indicate cross-slope currents transporting more sediments toward the deep layers. Since slope currents can affect ocean stratification through baroclinic instabilities, they can themselves generate oscillatory signals in the deep layer [64] and induce current reversals, which in turn, cause vertical displacements of the water as well as sediment resuspension, interacting with the continental slope. Hence, the two phenomena, i.e., internal oscillations and gravity currents, can coexist although hardly discernible from our data.

Finally, our study shows that the West Spitsbergen Shelf experiences high seasonal and interannual thermohaline variability associated with the inflows of AW and outflows of cold and fresh water from fjords. A large thermohaline variability can strongly influence the generation of dense water plumes on the shelf, as well as their properties. At the same time, a warming trend of AW emerges in agreement with previous studies [22,28,65]. Similarly, a slightly positive temperature trend appear also in the deep layer, which is consistent with the observed continuous warming of the deep waters in all sub-regions of the Nordic Seas [65].

In conclusion, our observations suggest that shelf-slope dynamics modulated by synoptic atmospheric forcing can increase the mixing rate between upper and deep layers along the west Spitsbergen continental slope, contributing to the slow modification of the deep layer (>800 m depth) along the west Svalbard margin, which is experiencing a slight tendency to become warmer and saltier. Further analyses are required to understand if prolonged injections of relatively warm water within the deep layer along the west Spitsbergen margin could potentially be responsible for future modifications of the abyssal waters in the Arctic Ocean.

Author Contributions: M.B. set the leading hypotheses of the work, performed data analysis, and wrote the main manuscript text. V.K., L.L., S.A. co-designed the research, participated in data analyses and interpretation and contributed to writing the text. A.R., L.U., I.G., T.S., R.S., F.N., contributed to data analyses and writing the manuscript. D.D., P.M., R.L., M.R., L.R., R.G.L., A.V., A.W., and A.B.-M. participated in data acquisition and interpretation. All authors reviewed the manuscript.

Conflicts of Interest: The authors declare no competing interests.

References

1. Skogseth, R.; Sandvik, A.D.; Asplin, L. Wind and tidal forcing on the meso-scale circulation in Storfjorden, Svalbard. *Cont. Shelf Res.* **2007**, *27*, 208–227. [CrossRef]
2. Nilsen, F.; Skogseth, R.; Vaardal-Lunde, J.; Inall, M. A Simple Shelf Circulation Model: Intrusion of Atlantic Water on the West Spitsbergen Shelf. *J. Phys. Oceanogr.* **2016**, *46*, 1209–1230. [CrossRef]
3. Onarheim, I.H.; Årthun, M. Toward an ice-free Barents Sea. *Geophys. Res. Lett.* **2017**, *44*, 8387–8395. [CrossRef]
4. Polyakov, I.V.; Pnyushkov, A.V.; Alkire, M.B.; Ashik, I.M.; Baumann, T.M.; Carmack, E.C.; Goszczko, I.; Guthrie, J.; Ivanov, V.V.; Kanzow, T.; et al. Greater role for Atlantic inflows on sea-ice loss in the Eurasian Basin of the Arctic Ocean. *Science* **2017**, *356*, 285–291. [CrossRef]
5. Backhaus, J. Formation and export of water masses produced in Arctic shelf polynyas—Process studies of oceanic convection. *ICES J. Mar. Sci.* **1997**, *54*, 366–382. [CrossRef]
6. Fohrmann, H.; Backhaus, J.O.; Blaume, F.; Rumohr, J. Sediments in Bottom-Arrested Gravity Plumes: Numerical Case Studies. *J. Phys. Oceanogr.* **1998**, *28*, 2250–2274. [CrossRef]

7. Rudels, B.; Björk, G.; Nilsson, J.; Winsor, P.; Lake, I.; Nohr, C. The interaction between waters from the Arctic Ocean and the Nordic Seas north of Fram Strait and along the East Greenland Current: Results from the Arctic Ocean-02 Oden expedition. *J. Mar. Syst.* **2005**, *55*, 1–30. [CrossRef]

8. Postlethwaite, C.F.; Morales Maqueda, M.A.; le Fouest, V.; Tattersall, G.R.; Holt, J.; Willmott, A.J. The effect of tides on dense water formation in Arctic shelf seas. *Ocean Sci.* **2011**, *7*, 203–217. [CrossRef]

9. Wobus, F.; Shapiro, G.I.; Huthnance, J.M.; Maqueda, M.A.M.; Aksenov, Y. Tidally induced lateral dispersion of the Storfjorden overflow plume. *Ocean Sci.* **2013**, *9*, 885–899. [CrossRef]

10. Wobus, F.; Shapiro, G.I.; Huthnance, J.M.; Maqueda, M.A.M. The piercing of the Atlantic Layer by an Arctic shelf water cascade in an idealised study inspired by the Storfjorden overflow in Svalbard. *Ocean Model.* **2013**, *71*, 54–65. [CrossRef]

11. Sanchez-Vidal, A.; Veres, O.; Langone, L.; Ferré, B.; Calafat, A.; Canals, M.; Durrieu de Madron, X.; Heussner, S.; Mienert, J.; Grimalt, J.O.; et al. Particle sources and downward fluxes in the eastern Fram strait under the influence of the west Spitsbergen current. *Deep Sea Res. Part Oceanogr. Res. Pap.* **2015**, *103*, 49–63. [CrossRef]

12. Bensi, M.; Kovačević, V.; Ursella, L.; Rebesco, M.; Langone, L.; Viola, A.; Mazzola, M.; Beszczynska-Möller, A.; Goszczko, I.; Soltwedel, T.; et al. Spitsbergen Oceanic and Atmospheric interactions—SOA. In *SESS Report 2018 The State of Environmental Science in Svalbard—An Annual Report*; Orr, E., Hansen, G., Lappalainen, H., Hübner, C., Lihavainen, H., Eds.; Longyearbyen, Svalbard Integrated Arctic Earth Observing System (SIOS): Longyearbyen, Norway, 2019; ISBN 978-82-691528-0-7.

13. Teigen, S.H.; Nilsen, F.; Gjevik, B. Barotropic instability in the West Spitsbergen Current. *J. Geophys. Res.* **2010**, *115*. [CrossRef]

14. Teigen, S.H.; Nilsen, F.; Skogseth, R.; Gjevik, B.; Beszczynska-Möller, A. Baroclinic instability in the West Spitsbergen Current. *J. Geophys. Res. Oceans* **2011**, *116*. [CrossRef]

15. Von Appen, W.-J.; Schauer, U.; Somavilla, R.; Bauerfeind, E.; Beszczynska-Möller, A. Exchange of warming deep waters across Fram Strait. *Deep Sea Res. Part Oceanogr. Res. Pap.* **2015**, *103*, 86–100. [CrossRef]

16. Van Haren, H.; Greinert, J. Turbulent high-latitude oceanic intrusions—Details of non-smooth apparent isopycnal transport West of Svalbard. *Ocean Dyn.* **2016**, *66*, 785–794. [CrossRef]

17. Fer, I.; Ådlandsvik, B. Descent and mixing of the overflow plume from Storfjord in Svalbard: An idealized numerical model study. *Ocean Sci.* **2008**, *4*, 115–132. [CrossRef]

18. Nilsen, F.; Cottier, F.; Skogseth, R.; Mattsson, S. Fjord–shelf exchanges controlled by ice and brine production: The interannual variation of Atlantic Water in Isfjorden, Svalbard. *Cont. Shelf Res.* **2008**, *28*, 1838–1853. [CrossRef]

19. Tverberg, V.; Nøst, O.A.; Lydersen, C.; Kovacs, K.M. Winter sea ice melting in the Atlantic Water subduction area, Svalbard Norway. *J. Geophys. Res. Oceans* **2014**, *119*, 5945–5967. [CrossRef]

20. Tverberg, V.; Skogseth, R.; Cottier, F.; Sundfjord, A.; Walczowski, W.; Inall, M.; Falck, E.; Pavlova, O.; Nilsen, F. The Kongsfjorden Transect: Seasonal and inter-annual variability in hydrography. In *The Ecosystem Kongsfjorden, Svalbard*; Hop, H., Wiencke, C., Eds.; Adv. Polar Ecol.; Springer: Cham, Switzerland, 2019; p. 562. ISBN 978-3-319-46423-7.

21. Aagaard, K.; Foldvik, A.; Hillman, S.R. The West Spitsbergen Current: Disposition and water mass transformation. *J. Geophys. Res. Oceans* **1987**, *92*, 3778–3784. [CrossRef]

22. Beszczynska-Möller, A.; Fahrbach, E.; Schauer, U.; Hansen, E. Variability in Atlantic water temperature and transport at the entrance to the Arctic Ocean, 1997–2010. *ICES J. Mar. Sci.* **2012**, *69*, 852–863. [CrossRef]

23. Boyd, T.J.; D'Asaro, E.A. Cooling of the West Spitsbergen Current: Wintertime observations west of Svalbard. *J. Geophys. Res. Oceans* **1994**, *99*, 22597–22618. [CrossRef]

24. Swift, J.H.; Koltermann, K.P. The origin of Norwegian Sea deep water. *J. Geophys. Res. Oceans* **1988**, *93*, 3563–3569. [CrossRef]

25. Sternal, B.; Szczuciski, W.; Forwick, M.; Zajączkowski, M.; Lorenc, S.; Przytarska, J. Postglacial variability in near-bottom current speed on the continental shelf off south-west Spitsbergen. *J. Quat. Sci.* **2014**, *29*, 767–777. [CrossRef]

26. Menze, S.; Ingvaldsen, R.B.; Haugan, P.; Fer, I.; Sundfjord, A.; Beszczynska-Moeller, A.; Falk-Petersen, S. Atlantic Water Pathways along the North-Western Svalbard Shelf Mapped Using Vessel-Mounted Current Profilers. *J. Geophys. Res. Oceans* **2019**, *124*. [CrossRef]

27. Polyakov, I.V.; Alekseev, G.V.; Timokhov, L.A.; Bhatt, U.S.; Colony, R.L.; Simmons, H.L.; Walsh, D.; Walsh, J.E.; Zakharov, V.F. Variability of the Intermediate Atlantic Water of the Arctic Ocean over the Last 100 Years. *J. Clim.* **2004**, *17*, 4485–4497. [CrossRef]

28. Walczowski, W.; Beszczynska-Möller, A.; Wieczorek, P.; Merchel, M.; Grynczel, A. Oceanographic observations in the Nordic Sea and Fram Strait in 2016 under the IO PAN long-term monitoring program AREX. *Oceanologia* **2017**, *59*, 187–194. [CrossRef]

29. Polyakov, I.V.; Bhatt, U.S.; Walsh, J.E.; Abrahamsen, E.P.; Pnyushkov, A.V.; Wassmann, P.F. Recent oceanic changes in the Arctic in the context of long-term observations. *Ecol. Appl.* **2013**, *23*, 1745–1764. [CrossRef] [PubMed]

30. Walczowski, W.; Piechura, J. Pathways of the Greenland Sea warming. *Geophys. Res. Lett.* **2007**, *34*, L10608. [CrossRef]

31. Promińska, A.; Cisek, M.; Walczowski, W. Kongsfjorden and Hornsund hydrography–comparative study based on a multiyear survey in fjords of west Spitsbergen. *Oceanologia* **2017**, *59*, 397–412. [CrossRef]

32. Oldenburg, D.; Armour, K.C.; Thompson, L.; Bitz, C.M. Distinct Mechanisms of Ocean Heat Transport into the Arctic Under Internal Variability and Climate Change. *Geophys. Res. Lett.* **2018**, *45*, 7692–7700. [CrossRef]

33. Lien, V.S.; Vikebø, F.B.; Skagseth, Ø. One mechanism contributing to co-variability of the Atlantic inflow branches to the Arctic. *Nat. Commun.* **2013**, *4*, 1488. [CrossRef] [PubMed]

34. Polyakov, I.V.; Beszczynska, A.; Carmack, E.C.; Dmitrenko, I.A.; Fahrbach, E.; Frolov, I.E.; Gerdes, R.; Hansen, E.; Holfort, J.; Ivanov, V.V.; et al. One more step toward a warmer Arctic. *Geophys. Res. Lett.* **2005**, *32*. [CrossRef]

35. Walczowski, W.; Piechura, J.; Goszczko, I.; Wieczorek, P. Changes in Atlantic water properties: An important factor in the European Arctic marine climate. *ICES J. Mar. Sci.* **2012**, *69*, 864–869. [CrossRef]

36. Haarpaintner, J. The Storfjorden polynya: ERS-2 SAR observations and overview. *Polar Res.* **1999**, *18*, 175–182. [CrossRef]

37. Haarpaintner, J.; Gascard, J.-C.; Haugan, P.M. Ice production and brine formation in Storfjorden, Svalbard. *J. Geophys. Res. Oceans* **2001**, *106*, 14001–14013. [CrossRef]

38. Skogseth, R.; Haugan, P.M.; Jakobsson, M. Watermass transformations in Storfjorden. *Cont. Shelf Res.* **2005**, *25*, 667–695. [CrossRef]

39. Jardon, F.P.; Vivier, F.; Bouruet-Aubertot, P.; Lourenço, A.; Cuypers, Y.; Willmes, S. Ice production in Storfjorden (Svalbard) estimated from a model based on AMSR-E observations: Impact on water mass properties. *J. Geophys. Res. Oceans* **2014**, *119*, 377–393. [CrossRef]

40. Preußer, A.; Willmes, S.; Heinemann, G.; Paul, S. Thin-ice dynamics and ice production in the Storfjorden polynya for winter-seasons 2002/2003–2013/2014 using MODIS thermal infrared imagery. *Cryosphere* **2015**, *9*, 1063–1073. [CrossRef]

41. Quadfasel, D.; Rudels, B.; Kurz, K. Outflow of dense water from a Svalbard fjord into the Fram Strait. *Deep Sea Res. Part Oceanogr. Res. Pap.* **1988**, *35*, 1143–1150. [CrossRef]

42. Jungclaus, J.H.; Backhaus, J.O.; Fohrmann, H. Outflow of dense water from the Storfjord in Svalbard: A numerical model study. *J. Geophys. Res.* **1995**, *100*, 24719. [CrossRef]

43. Shaw, P.-T.; Chao, S.-Y. Effects of a baroclinic current on a sinking dense water plume from a submarine canyon and heton shedding. *Deep Sea Res. Part Oceanogr. Res. Pap.* **2003**, *50*, 357–370. [CrossRef]

44. Inall, M.E.; Nilsen, F.; Cottier, F.R.; Daae, R. Shelf/fjord exchange driven by coastal-trapped waves in the Arctic. *J. Geophys. Res. Oceans* **2015**, *120*, 8283–8303. [CrossRef]

45. Nilsen, F.; Gjevik, B.; Schauer, U. Cooling of the West Spitsbergen Current: Isopycnal diffusion by topographic vorticity waves. *J. Geophys. Res.* **2006**, *111*, C08012. [CrossRef]

46. Cacchione, D.A.; Pratson, L.F.; Ogston, A.S. The shaping of continental slopes by internal tides. *Science* **2002**, *296*, 724–727. [CrossRef]

47. Cacchione, D.A.; Drake, D.E. Nepheloid layers and internal waves over continental shelves and slopes. *Geo-Mar. Lett.* **1986**, *6*, 147–152. [CrossRef]

48. Akimova, A.; Schauer, U.; Danilov, S.; Núñez-Riboni, I. The role of the deep mixing in the Storfjorden shelf water plume. *Deep Sea Res. Part Oceanogr. Res. Pap.* **2011**, *58*, 403–414. [CrossRef]

49. Rebesco, M.; Wåhlin, A.; Laberg, J.S.; Schauer, U.; Beszczynska-Möller, A.; Lucchi, R.G.; Noormets, R.; Accettella, D.; Zarayskaya, Y.; Diviacco, P. Quaternary contourite drifts of the Western Spitsbergen margin. *Deep Sea Res. Part Oceanogr. Res. Pap.* **2013**, *79*, 156–168. [CrossRef]

50. Etling, D.; Gelhardt, F.; Schrader, U.; Brennecke, F.; Kühn, G.; d'Hieres, G.C.; Didelle, H. Experiments with density currents on a sloping bottom in a rotating fluid. *Dyn. Atmos. Oceans* **2000**, *31*, 139–164. [CrossRef]

51. Pawlowicz, R.; Beardsley, B.; Lentz, S. Classical tidal harmonic analysis including error estimates in MATLAB using T_TIDE. *Comput. Geosci.* **2002**, *28*, 929–937. [CrossRef]

52. Carpenter, J.H. The Accuracy of the Winkler Method for Dissolved Oxygen Analysis1. *Limnol. Oceanogr.* **1965**, *10*, 135–140. [CrossRef]

53. Schlitzer, R. Ocean Data View. 2018. Available online: http://odv.awi.de/ (accessed on 1 October 2018).

54. Artegiani, A.; Paschini, E.; Russo, A.; Bregant, D.; Raicich, F.; Pinardi, N. The Adriatic Sea General Circulation. Part I: Air–Sea Interactions and Water Mass Structure. *J. Phys. Oceanogr.* **1997**, *27*, 1492–1514. [CrossRef]

55. Torrence, C.; Compo, G.P. A practical guide to wavelet analysis. *Bull. Am. Meteorol. Soc.* **1998**, *79*, 61–78. [CrossRef]

56. Saloranta, T.M.; Svendsen, H. Across the Arctic front west of Spitsbergen: High-resolution CTD sections from 1998–2000. *Polar Res.* **2001**, *20*, 177–184.

57. Chatterjee, S.; Raj, R.P.; Bertino, L.; Skagseth, Ø.; Ravichandran, M.; Johannessen, O.M. Role of Greenland Sea Gyre Circulation on Atlantic Water Temperature Variability in the Fram Strait. *Geophys. Res. Lett.* **2018**, *45*, 8399–8406. [CrossRef]

58. Zhao, M.; Timmermans, M.-L.; Cole, S.; Krishfield, R.; Proshutinsky, A.; Toole, J. Characterizing the eddy field in the Arctic Ocean halocline. *J. Geophys. Res. Oceans* **2014**, *119*, 8800–8817. [CrossRef]

59. Lien, V.S.; Gusdal, Y.; Vikebø, F.B. Along-shelf hydrographic anomalies in the Nordic Seas (1960–2011): Locally generated or advective signals? *Ocean Dyn.* **2014**, *64*, 1047–1059. [CrossRef]

60. Skeie, P.; Gronaas, S. Strongly stratified easterly flows across Spitsbergen. *Tellus A* **2000**, *52*, 473–486. [CrossRef]

61. Häkkinen, S.; Cavalieri, D.J. A study of oceanic surface heat fluxes in the Greenland, Norwegian, and Barents Seas. *J. Geophys. Res. Oceans* **1989**, *94*, 6145–6157. [CrossRef]

62. Akiyama, J.; Stefan, H. Turbidity Current with Erosion and Deposition. *J. Hydraul. Eng.* **1985**, *111*, 1473–1496. [CrossRef]

63. Kämpf, J.; Backhaus, J.O.; Fohrmann, H. Sediment-induced slope convection: Two-dimensional numerical case studies. *J. Geophys. Res. Oceans* **1999**, *104*, 20509–20522. [CrossRef]

64. Gill, A. *Atmosphere-Ocean Dynamics*, 1st ed.; Academic Press: San Diego, CA, USA, 1982; Volume 30, ISBN 978-0-08-057052-5.

65. González-Pola, C.; Larsen, K.M.; Fratantoni, P.; Beszczynska-Möller, A.; Hughes, S.L. *ICES Report on Ocean Climate 2016*; ICES Cooperative Research Report No. 339; International Council for the Exploration of the Sea (ICES), Conseil International pour l'Exploration de la Mer (CIEM): Copenhagen, Denmark, 2018; p. 110.